LASER INTERFEROMETER GRAVITATIONAL WAVE OBSERVATORY
- LIGO -
CALIFORNIA INSTITUTE OF TECHNOLOGY
MASSACHUSETTS INSTITUTE OF TECHNOLOGY

Design Document LIGO-T980064-00 - D 17 July 1998

ASC Wavefront Sensing Final Design

ISC group

Distribution of this draft:

ASC FDR Committee

This is an internal working note
of the LIGO Project.

California Institute of Technology
LIGO Project - MS 51-33
Pasadena CA 91125
Phone (818) 395-2129
Fax (818) 304-9834
E-mail: info@ligo.caltech.edu

Massachusetts Institute of Technology
LIGO Project - MS 20B-145
Cambridge, MA 01239
Phone (617) 253-4824
Fax (617) 253-7014
E-mail: info@ligo.mit.edu

WWW: http://www.ligo.caltech.edu/

1. INTRODUCTION AND DESIGN OVERVIEW

1.1. ASC/WFS scope and context

The WFS component of the LIGO Detector Alignment Sensing and Control (ASC) system comprises optoelectronic sensing hardware, control dynamics and process specifications, and supervisory state algorithms which attain and maintain optical alignment of a LIGO interferometer's core and input optics during observatory observations (referred to herein as the "Detection" operating mode). The system integrates inputs from two sensor types, Wavefront Sensing and Beam Centering, to:

- optimize the modal coupling between subcavities of the fully coupled interferometer, thus maximizing the circulating power and signal, minimizing shot noise, and minimizing susceptibility to parametric noise infiltration, and simultaneously;
- maintain the physical centering of this optimized mode on the core optics, to minimize lever-arm coupling of thermal angular fluctuations into critical interferometer lengths.

The sensed alignment and centering error signals are filtered, transformed into the basis of individual optic element rotations, and applied as pitch and yaw angle correction torques through their respective suspension controllers (or tip/tilt mirrors, in the case of IO mode cleaner input alignment).

Beam video imaging sensors are provided as part of ASC/WFS to permit characterization of the circulating mode, diagnostic measurements, and operational monitoring of resonant states. All three sensor types are integrated (along with LSC length sensors and some COS components) onto ISC Tables and ETM Transmission Monitor platforms, located in the LIGO corner LVEA and mid/end VEA, respectively. The ASC/WFS subsystem also provides diagnostic input and output hooks for test and characterization of itself and other subsystems (e.g., SUS, PSL, IO, etc.).

The ASC/WFS component relies on interferometric readouts; the job of initially attaining sufficient mirror alignment to obtain optical interference is performed by the ASC/IAS (Initial Alignment System) component, described separately in LIGO-T980019-00-D, *ASC Initial Alignment Subsystem Final Design*. The inextricable function of attaining and maintaining optical pathlengths and laser wavelengths commensurate with cavity resonance is performed by the LSC (Length Sensing and Control) system, which is described in LIGO-T970122, *Length Sensing and Control Subsystem Preliminary Design*. The se relationships are depicted in Figure 1.

Electronics hardware and software which implement the control signal processing and supervisory state algorithms described in the Design will be developed collaboratively with LIGO CDS during the implementation phase; these will be documented in the CDS ASC/WFS Final Design.

Figure 1: ASC/WFS context within LIGO Detector

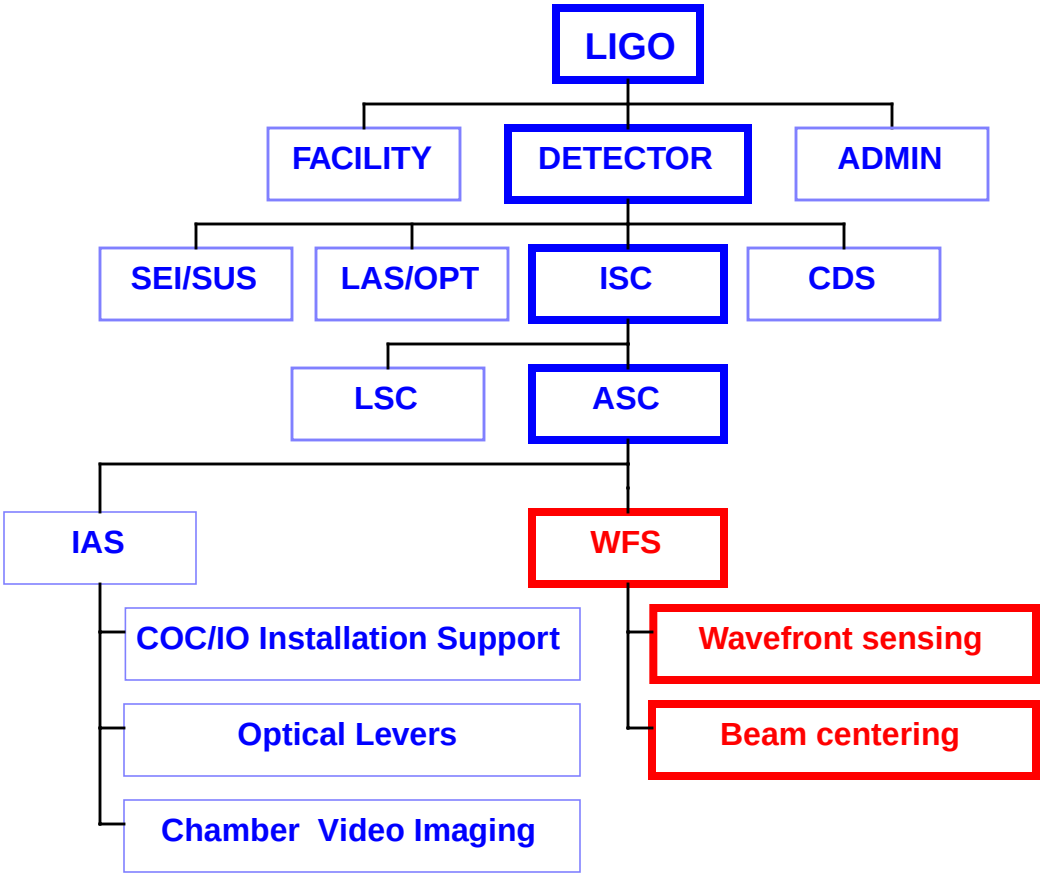

1.2. Significant departures from the preliminary design

The WFS design presented in LIGO-T970060-00-D, ASC Preliminary Design, has been changed relatively little. Beyond normal detailing and specification appropriate to completion at final design level, the following updates may be worth noting:

- We incorporated the "as-built" LOS suspension driver output filter into the overall WFS control model. In retrospect, it now appears this filter was not an optimal choice from the standpoint of loop gain and phase margin. One result of this is that...
- Exercising the revised control designs against three samples of expected seismic motion (Hanford and Livingston under two different conditions) reveals that the RMS angle requirement is slightly exceeded in the noisiest Livingston circumstances (Section 4.4.1.).
- Results of digital processing, ADC and DAC tests have been incorporated in a proposed distribution of whitening, dewhitening and digital filter functions, as well as in the allocation of phase margin to digital processing delays (Section 4.4.2.).
- The quadrant photodiode originally chosen for wavefront sensors was discontinued by the maker (actually, an unannounced design change which rendered it unusable). An alternate vendor was found and qualified through testing (Section 4.2.3.).

2. ASC/WFS SUBSYSTEM INTERFACES

2.1. COS

It is assumed that interferometer output beams and sample beams originating in vacuum are collimated and positioned, and have maximum wavefront aberrations, as described in LIGO-T980071-02, *Core Opics Support DRD,* LIGO-T980010-01, *Core Optics Support Preliminary Design,* and LIGO-T980054-00-D, *PO Beam Waist Size and Location on the ISC Table*.

2.2. SUS

Control inputs for angular control of core optics are as specified in T960151-01, *Large and Small Optics Suspension Electronics Design Requirements,* and T970113-00, *Large and Small Optics Suspension Electronics Preliminary Design.*

2.3. SEI control operation

To compensate for long term alignment drifts (due, e.g., to stack settling), SEI will provide off-line control command inputs for translating the stack transverse to the optic axis (for long term beam centering control) and for rotating the stack about the vertical (for long term optic yaw control). The approximate ranges of these actuators are given in the SEI DRD, T960065-03. Specifications for the control interface are still TBD.

2.4. IOO control operation

The ASC design for the mode cleaner (MC) alignment calls for control inputs for the direction of the MC input beam, in the basis of input beam angle and position (reference plane at the MC waist). These are specified in LIGO-T980009-00-D, *Input Optics Final Design*, and T980040-00-C, *Input Optics CDS Preliminary Design.*

3. ISC LOCK ACQUISITION PROCEDURE

3.1. Overview

Interferometer lock acquisition involves sequential phasing of initial alignment (ASC IAS; see *ASC Initial Alignment Procedures,* LIGO-T970151-00-D, and *Initial Alignment System Final Design,* LIGO-T980019-00-D) and wavefront sensing (WFS) controls in concert with activation of cavity length (LSC) controls. According to this acquisition procedure, interferometer sub-cavities are sequentially brought into resonance. The planned alignment procedure outlined below will align these sub-cavities well enough to permit length locking to proceed at each stage. We will then subsequently use wavefront sensing to refine this alignment in preparation for the fol-

lowing stage, finally ending with all lenght and alignment controls active on a fully resonant interferometer. For more on the acquisition process, see the *LSC Preliminary Design*, LIGO-T970122-00.

3.2. Wide angle behavior of WFS readouts

Modal model simulations extended to many modes and applied at large angular misalignment are described in [T960191-00-D]. Three main topics were investigated: the modal decomposition of the electric fields, the servo-stability of the length sensing signals and the linearity of the wavefront sensing signals when the interferometer is close to resonance. The investigations were made in the basis which is diagonal for the degradation of the gravitational-wave readout: u_1 to u_5 as defined in Appendix 1. Table 1 summarizes the findings. Even though the angles for which the power in the recycling and the in-line arm cavity has dropped by factor of two and the stability boundaries for longitudinal and angular misalignment are vastly different in different directions, they are usually very similar in absolute values for each direction. The smallest limit for a stable alignment is obtained for a misalignment in the direction of u_1~1×10^{-7} rad. This misalignment involves only the recycling mirror and the ITMs, suggesting that during lock acquisition the recycling cavity should be aligned before the arm cavities are brought into resonance.

Table 1 Power degradation and decrease of servo stability due to large angular misalignments. For each principal angular direction the angle for which the power has degraded by half and the angle for which the length and alignment sensitivities have decreased by half are shown. The values are given in units of the arm cavity divergence angle which is ~10^{-5} rad.

Direction	$\frac{1}{2}$ *Recycling cavity power*		$\frac{1}{2}$ *Arm power*	*Stability (half gain point)*	
	sidebands	*carrier*	*carrier*	*LSC*	*ASC*
u_5	> 1	> 1	> 1	> 1	> 1
u_4	0.7	0.6	0.5	0.6	0.65
u_3	0.3	> 0.6	> 0.6	0.15	0.15
u_2	0.15	0.06	0.06	0.04	0.04
u_1	0.015	> 0.1	> 0.1	~0.01	~0.01

3.3. Sub-states of the IFO

We use the following definitions of interferometer substates, where the state number corresponds to the number of length degrees-of-freedom that are resonant:

- **State 2:** The recycling cavity is resonant for the main sidebands, and the Michelson is at the point of zero path length difference for the carrier (normal dark port condition, even

though there is very little carrier in the recycling cavity); carrier is nowhere resonant

- **State 3:** The conditions of state 2 hold, plus one of the arm cavities is resonant for the carrier
- **State 4:** The entire interferometer is resonant in the normal Detection Mode state.

3.3.1. Unlocked recycled Michelson - manual alignment

The recycled Michelson must be aligned well enough so that it can be locked in length. The first step will be to manually align the cavity consisting of the recycling mirror, the beamsplitter, and the on-line ITM (refer to Fig. 2a); the off-line ITM is given a large misalignment (the ETMs are also misaligned). The effect of the beamsplitter angles is insignificant, and this can be thought of as a (very lossy) two mirror cavity. An initial, relatively crude, alignment of this configuration is made by monitoring scattered light from the edge bevels of the the recycling mirror and on-line ITM as their angles are manually adjusted, and interpolating the approximate central position. The cavity length is then swept through several lambda by driving the RM, at a frequency of ~5 Hz. The power in the cavity is simultaneously monitored using the AR surface (ghost) beam from the ITM (using the dc readout of either an LSC photodetector or ASC wavefront sensor). The fringe contrast is then maximized by manually adjusting the pitch and yaw angles of the RM and ITM. This is done with the modulation index turned down (Γ~0.1) so there is no confusion from the different resonant lengths for the carrier and sidebands.

The maximum fringe contrast achievable in this configuration is 80%. Once something close to this is achieved, the off-line ITM is manually brought into alignment, so that its reflection interferes at the beamsplitter with the main beam (Fig. 2b). The off-line ITM alignment is optimized by monitoring the anti-symmetric port beam with a video camera (spatial interference fringes will be seen and will indicate the direction of misalignment), and the cavity power with the ITM ghost beam. The RM axial position is also driven in this phase, and the position of one of the ITMs may also be driven.

Once the power buildup in the recycling cavity is at least ~10% of the maximum possible level, the two length control loops are closed. The maximum possible level, as measured by the ITM

ghost beam detector, can be inferred from the signal level measured in the first step (paragraph) above and the mirror transmissions.

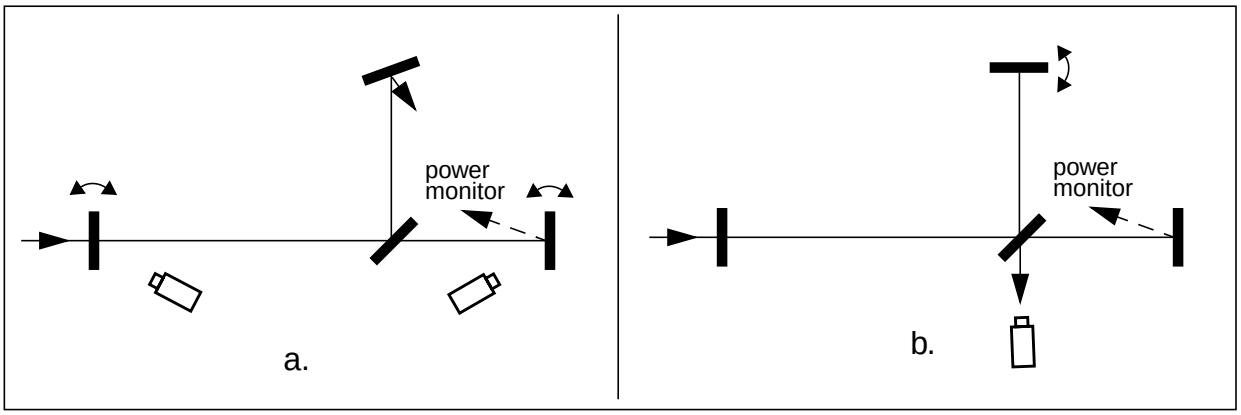

Figure 2 Steps involved in the manual alignment of the recycled Michelson. In step **a,** one of the ITM's is intentionally misaligned, and the other ITM and the RM are manually aligned by interpolating the beam position between the edge bevels (imaged in a video camera). In step b, the other ITM is then aligned, using the spot pattern at the anti-symmetric port for guidance.

3.3.2. Resonant recycled Michelson (state 2)

Once the recycled Michelson is locked in length by LSC, ASC will use the wavefront sensor system to further optimize its alignment. Because of the degeneracy of the recycling cavity, only two degrees-of-freedom can be aligned using the wavefront sensor signals - these are the ITM differential alignment, and the combination of recycling mirror and ITM common mode alignment corresponding to the eigenvector $\boldsymbol{u_1}$ (refer to Appendix 1 or to ref. [4]).

The wavefront sensor signals 2a and 2b (coming from the I &Q phases of a single head at the reflection port) detect the same angle combinations as in Detection mode, the only difference being that in State 2 the signal strength (W/rad) is roughly 3× larger than in Detection mode. We thus can close the loops on these two degrees-of-freedom using the same transformation matrix as in Detection mode, using the acquisition servo loop described in section 4.4.3. We expect to be able to control these d.o.f. to 10^{-8} rad_{rms} or better.

The on- and off-line beams are then centered on the two ETM transmission quadrant monitors. For the initial alignment, this will begin by getting the beams into the ETM stations, as described in the *IAS Final Design* T980019-00-D. The arm carrying the on-line beam will be monitored first. The input beam direction will be varied (using the IOO telescope mirrors) until the beam is detected in the on-line arm ETM beam tube manifold, using a port-mounted video camera (viewing the manifold interior, on which is projected the reflection from the COS Brewster-angle beam dump). The beam is then manually directed to hit the ETM. The beam transmitted by the ETM is now picked up by the transmission quadrant monitor, and the beam can be centered on this monitor. The same procedure is then applied to the off-line beam, the only difference being that the beamsplitter angles are adjusted to direct the beam in the off-line arm.

Just before transitioning to State 3, the wavefront sensor servos will be disengaged so that they do not have to deal with the transients involved with going from State 2 to State3. Since these optics are all in the LVEA area, we expect that the alignment will remain within 10^{-7} rad of the controlled level over reasonably long times scales (≥ 100 seconds).

3.3.3. Recycled MI + one arm locked (state 3)

One of the ETMs is now aligned manually. It is first brought back to the orientation determined during the initial (installation) alignment, by referring to the optical lever and suspension sensor signals. If the installation alignment is not good enough that the reflected beam from the ETM falls on the ITM surface, the returning beam will be found in the ITM beam manifuld using the video cameras and manual adjustments of the ETM orientation. Once the return beam is on the ITM surface, the ETM orientation will be further adjusted by interpolating the spot between the edge bevels, using the IAS chamber video camera directed at that mirror; we expect this will bring the ETM orientation within about ~10^{-6} rad of optimal.

At this point the length locking can proceed to state 3, such that the carrier is locked in the one arm that is now aligned. The interferometer is then more optimally aligned using the relevant wavefront sensor signals, either by manually adjusting mirror angles, or possibly by closing some of the alignment loops.

3.3.4. Full IFO locked (state 4)

The other, until now misaligned ETM is now brought back into rough alignment in the same way as the first ETM. At this point the length locking can proceed to state 4 - the final state where the full interferometer is resonant. The wavefront sensor alignment loops are then closed (either manually or in response to a trigger from the LSC signaling lock acquisition), followed by the quadrant monitor centering loops.

3.3.5. Alternate procedure

Probably the major weakness in the above scenario is the extremely tight initial alignment tolerance and the potential that a given resonant state is completely disrupted (lock broken) as the new optic is brought into alignment, due to the transient excitation of higher order modes.

An alternative approach which has much appeal is to first lock and align the two arm cavities, in a manner which is at least somewhat immune to the phase conditions in the recycling cavity. Two possibilities are: locking the arm cavities just off their resonant peaks by using the ETM transmitted light power, compared to a measure of the cavity input light power; locking the arm cavities in transmission at their resonances by using a length dither to generate an error signal.

The second method may be difficult (though it was used successfully to lock the first table-top full LIGO-like interferometer in a controlled manner), because the dither frequencies for the two cavities must be widely separated to avoid signal cross-coupling, but also must not be too high above

the arm cavity pole frequency to retain a reasonable signal size; these considerations may severely limit the bandwidth of the loops. Advantages of this approach are that the cavities are locked to the center of their resonances, and that the loops can be completely local to the end stations (no information needed from the vertex detectors).

The side-of-fringe locking approach may be more promising, since there is no such bandwidth limitation. The error signal for a cavity would be derived by comparing the cavity's transmitted light with a sample of the light entering the cavity (the recycling cavity pick-off beam). The relative gains of the two channels are adjusted so that a zero error signal occurs when the cavity is slightly off resonance.

4. DETECTION MODE CONTROL DESIGN

4.1. Sensor configuration

Fig. 3 shows the functional layout of the ASC sensors, an equipment location layout for the ASC hardware is shown in Figure 4, and a schematic optical layout for an ISC optical table is shown in XXX. The wavefront sensors and quadrant position detectors are discussed in detail in the following sections. Video cameras are used to detect directly samples of the beam at five locations (as shown in Figure 3): the two ETM transmission beams; the anti-symmetric port beam; the reflected beam; the recycling cavity pick-off beam. These units have no lenses, but do include fixed attenuators. The cameras are Sony model XC-75, 1/2″ CCD, B&W. They will be mounted on the ISC optical tables in the LVEA and at the end stations, on adapted, optical lever-type tables.

.

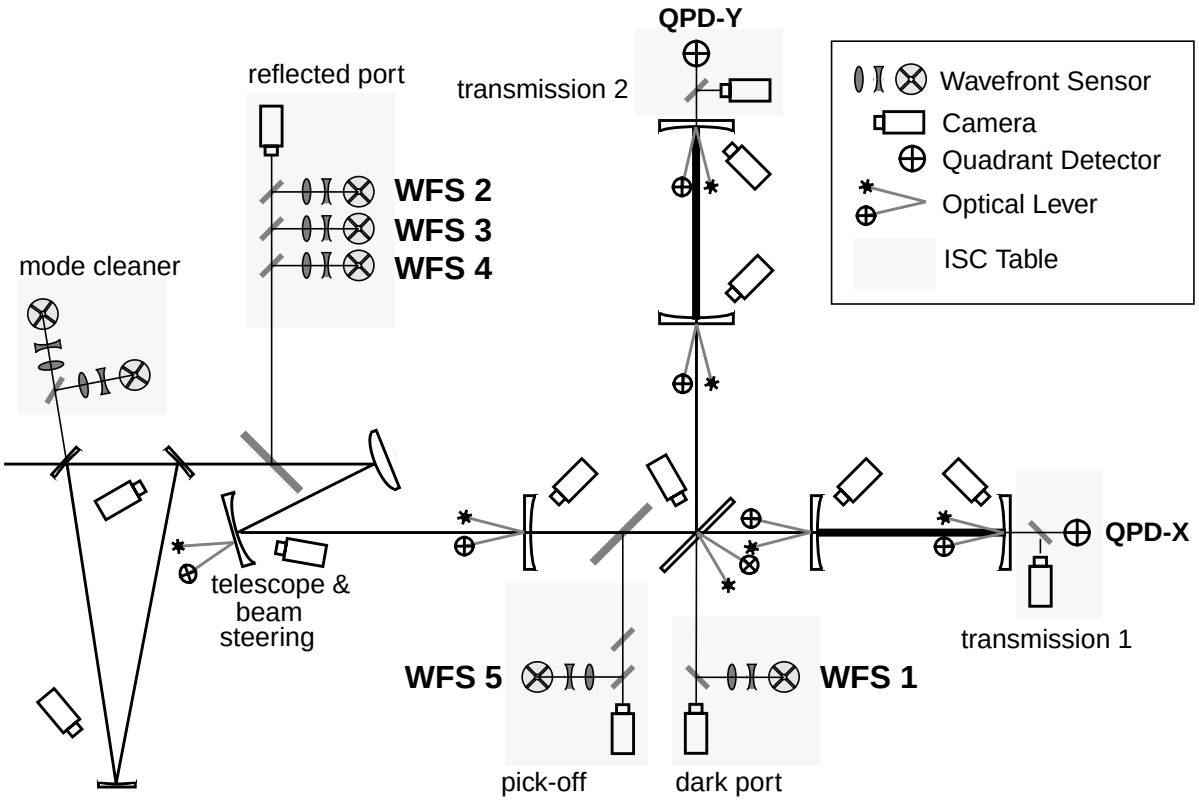

Figure 3 Functional layout of the ASC sensors. The 'pick-off' represents a beam from one of the ITM, or the BS, AR surfaces. The 'symmetric port' is representative of a sample of the interferometer reflected light.

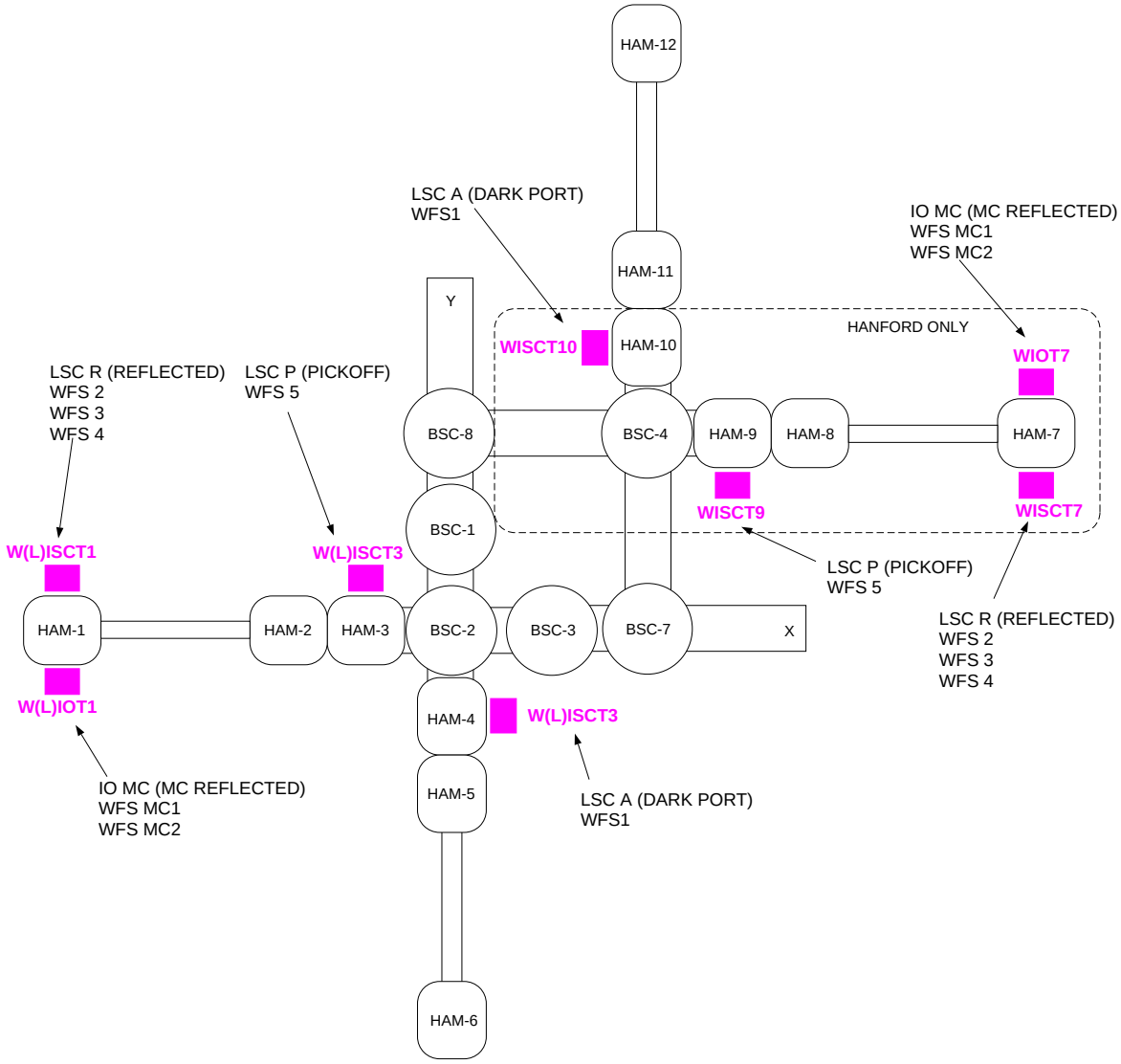

Figure 4 ASC equipment location schematic; vertex station at Hanford (Livingston designations similar except diagonal section, as indicated).

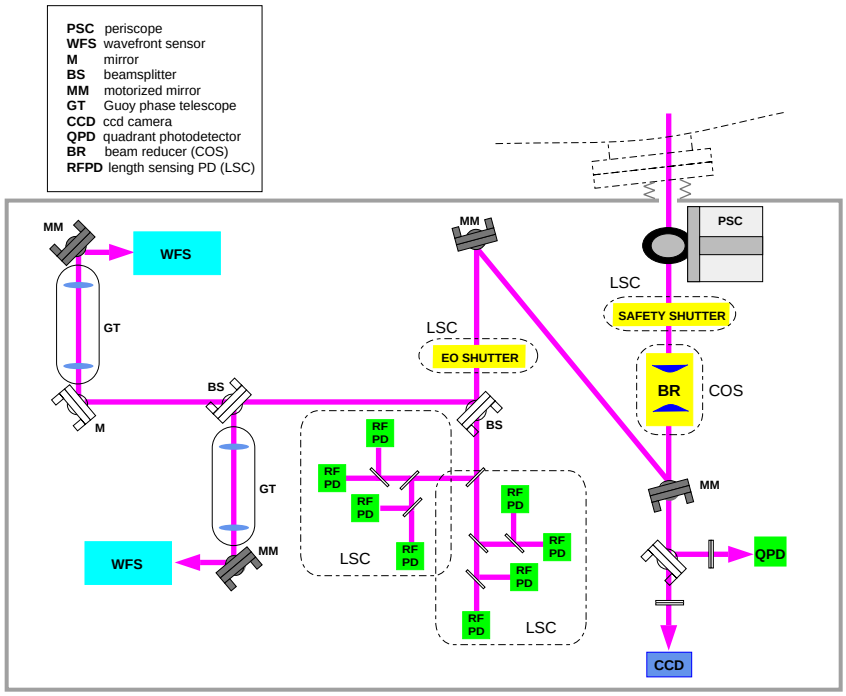

Schematic ISC optical table layout (dark port components only). The assembly is shielded by a light-tight safety/dust/thermal enclosure . Gasketed bulkhead feedthroughs pass signal and power wiring through the enclosure wall. The beam entry path from the vacuum port (top) is shielded by a bellows which seals to the rim of the vacuum view-port. A rigid periscope inside the enclosure drops the beam from port height (approximately 70” above the floor) to convenient working height on the optical bench. LSC and COS components are indicated by dashed boxes. This table will also include components to handle the P (pickoff) beam and the

4.2. Wavefront Sensor Design

At a particular port the wavefront sensor signal in general depends on all five degrees-of-freedom (in one dimension), and it can be written as:

$$WFS(\phi_d, \phi_g, \Theta, \Gamma) \;=\; P\, f(\Gamma)\, f_{\text{split}}\, k_{PD}^{10} \sum_{i=1}^{5} A_i \Theta_i \cos(\eta - \eta_{0i}) \cos(\omega_m t - \phi_{0i}) \qquad (1)$$

where for the *i*th angular d.o.f., Θ_i is the normalized misalignment angle[1], η_{0i} is the Guoy phase at the output port, η the Guoy phase shift added by the WFS telescope, ϕ_{0i} the phase of signal at the

1. Normalized to the beam divergence angle: $\Theta_i = (\pi\omega_0/\lambda)\theta_i^{\text{real}}$.

modulation frequency ω_m. The coefficient A_i is the rf-modulated component of the optical intensity due to the interference of TEM_{00} and TEM_{10} modes, integrated over a half-plane detector[1]. The units of A_i are watts, and it is normalized to 1 W of total input power; the modulation index is incorporated in the factor $f(\Gamma) \equiv 2 J_0(\Gamma) J_1(\Gamma)$, which for low modulation index reduces to $f(\Gamma) \approx \Gamma$ (A_i is independent of the modulation index). The input power is *P,* the fraction of a particular port's light that is directed to the wavefront sensor is f_{split}, and k_{PD}^{10} is a less-than-unity factor which accounts for the difference between the specific photodiode geometry and the idealized half-plane detector.

	Angular Degree-of-Freedom									
Port	**ΔETM**		**ΔITM**		**$\overline{\text{ETM}}$**		**$\overline{\text{ITM}}$**		**RM**	
Dark	**-25.0**		**-11.4**		-9.9×10^{-6}		-4.5×10^{-6}		1.2×10^{-3}	
	Q	90°	Q	90°∞	Q	156°	Q	156°	Q	90°
Reflected	2.3×10^{-2}		**-1.37**		-0.73		**6.21**		**-9.60**	
	Q	144°	Q	144°	I	97°	I	146°	I	146°
Recycling cavity	1.84×10^{-3}		**-0.11**		1.43×10^{-2}		**0.52**		**-0.72**	
	Q	144°	Q	144°	I	61°	I	143°	I	144°
Reflected - NR sideband	1.3×10^{-4}		-1.7×10^{-4}		**-2.11**		**-0.965**		**1.93**	
	I	-26°	I	95°	I	90°	I	90°	I	0°

Table 2 Matrix of Wavefront Sensor signals. Top entry in each cell is A_i (with significant values in boldface), lower-left is rf-phase, and lower-right is the Guoy phase.

The matrix of WFS signals generated by the interferometer defined in Table 14 is given in Table 2. In each cell of the table, the top entry is A_i, the lower-left is the rf-phase (I and Q referring to in-phase and quadrature-phase), and the lower-right is the Guoy phase η_{0i} The A_i for the recycling cavity and arm reflection ports include a factor of 3×10^{-4}, the reflectivity of the ITM AR surfaces.

The splitting factors for the various sensor heads are chosen to make the signal sensitivity (amps of photocurrent per radian of mirror angle) be of the same order of magnitude for all the sensors (this uniform level of sensitivity cannot of course be obtained for both signals - I & Q phase - of sensor 2). This is done so that a common head design (in terms of transimpedance gain and gain range) can be used for all the sensors. This means that we detect relatively less light on the sensors with inherently stronger signals.

1. A half-plane detector is one that subtracts and integrates over two mirror-symmetric half-infinite planes located left and right of the *y*-axis.

The splitting factors and effective optical input power levels for the sensors are shown below.

Wavefront Sensor	*Splitting factor*	*Effective input power, P*	*f* (Γ)
WFS 1	0.001	P_{in} = 6 W	0.42
WFS 2	0.0024	P_{in} = 6 W	0.42
WFS 3	0.02	$J^2_0(0.45)\cdot P_{in}$ = 5.4 W	0.05
WFS 4	0.02	$J^2_0(0.45)\cdot P_{in}$ = 5.4 W	0.05
WFS 5	0.2	P_{in} = 6 W	0.42

4.2.1. WFS Error Signal Matrix

The matrix of WFS error signals is now determined by the parameters of Table 2, and the sensors and splitting factors defined above. A remaining parameter in Equation (1) is the photodiode factor k^{10}_{PD}. We take a quadrant photodiode, for which k^{10}_{PD} = 0.70; the choice of photodiode geometry is discussed in section 4.2.2. below. The other remaining parameters in Equation (1) are the demodulator and Guoy phases. In practice neither phase can be set precisely to the desired value. The assumption is made that the demodulator phase can be set within 1° of the desired phase[1], and that the Guoy phase can be set within 5° of the desired phase. The error signal matrix resulting from these choices is shown in Table 3. The entries correspond to the level of rf-optical power per normalized angle; multiplying them by the photodiode responsivity gives the actual rf-photo-

1. Each WFS signal will be demodulated in I and Q phase; the resulting demodulated signals will be processed in software to extract the appropriate phase. This is how we believe we can achieve this precision.

current per normalized angle. Any value which was less than 0.01 of the largest value was set to zero.

M_{ij}	***Angular Degree-of-Freedom***					
Wavefront Sensor	**ΔETM**	**ΔITM**	**$\overline{\text{ETM}}$**	**$\overline{\text{ITM}}$**	**RM**	**u_i**
WFS 1	**-0.044**	**-0.02**	0	0	0	-0.048 u_2
WFS 2a	0	0	-2.0×10^{-3}	**0.026**	**-0.041**	-0.048 u_1
WFS 2b	9.6×10^{-5}	$\mathbf{-5.8 \times 10^{-3}}$	0	4.6×10^{-4}	-7.0×10^{-4}	(-0.14 u_1 - 0.40 u_2 - 0.91 u_3)(0.006)
WFS 3	0	0	-7.0×10^{-4}	-3.2×10^{-4}	$\mathbf{7.3 \times 10^{-3}}$	(0.83 u_1 + 0.13 u_4 - 0.54 u_5)(0.0073)
WFS 4	0	0	$\mathbf{-8.0 \times 10^{-3}}$	$\mathbf{-3.7 \times 10^{-3}}$	6.4×10^{-4}	(0.70 u_1 - 0.46 u_4 + 0.55 u_5)(0.0038)
WFS 5	6.5×10^{-4}	**-0.039**	0	3.2×10^{-3}	-4.4×10^{-3}	(-0.14 u_1 - 0.40 u_2 - 0.91 u_3)(0.04)

Table 3 Matrix of misalignment error signals, with the sensor locations and design parameters given in sections 4.1. and 4.2.. Matrix elements are labelled M_{ij}, where *i* refers to the WFS # (1, 2a, 2b, 3, 4, 5) and *j* refers to the angular d.o.f., in the order shown in the table. Units are Watts per normalized angle**.** The u_i are defined in Appendix 1.

4.2.2. Wavefront Processing Unit

A block diagram of a wavefront processing unit is shown in Figure 5. The unit includes: the sensor head and Guoy phase telescope, with motorized mirror mount for remote beam centering; the

demodulators for the rf-signals; ADCs for the dc and demodulated-rf signals; a signal processing unit; state control outputs and status inputs.

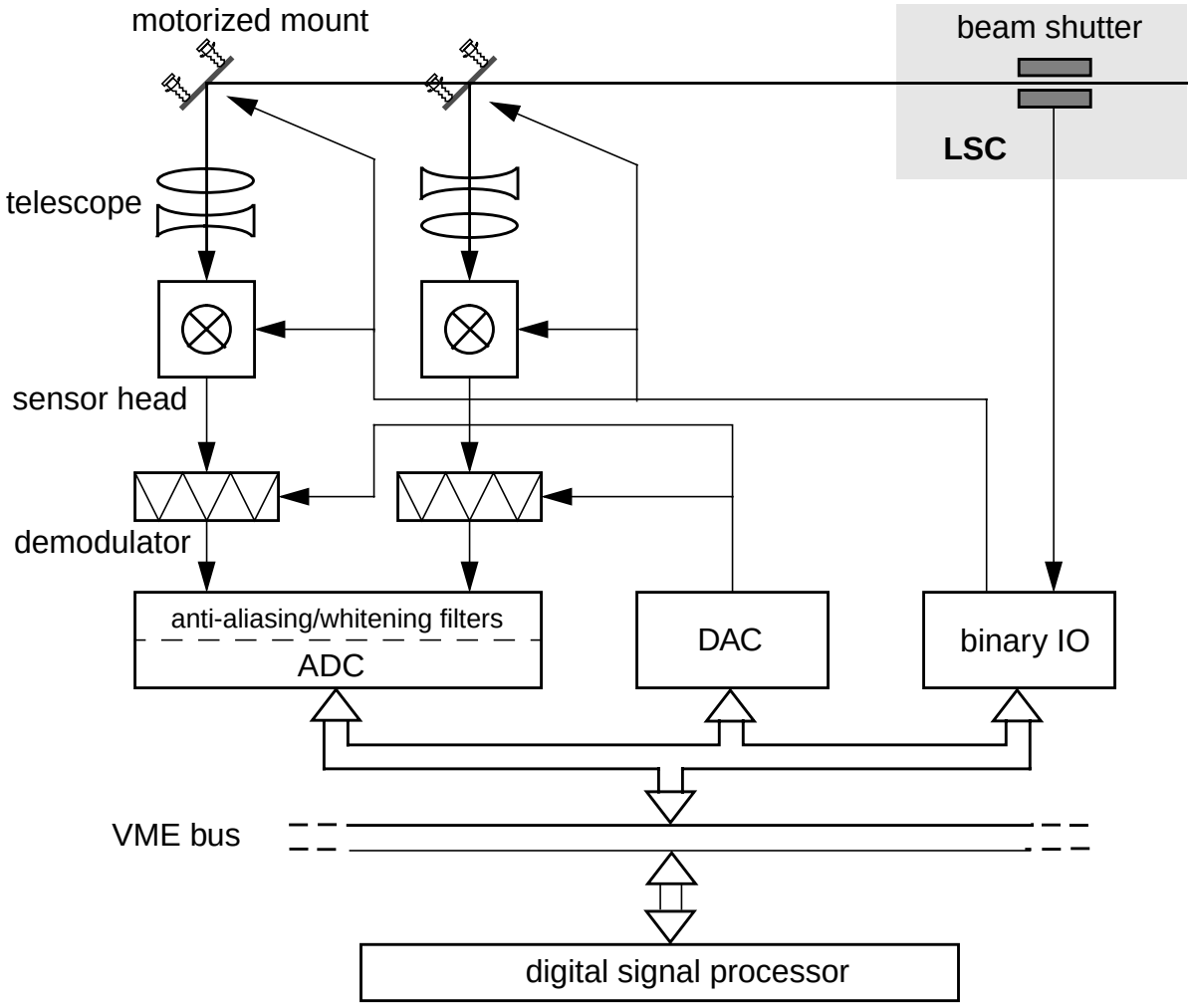

Figure 5 Wavefront Processing Unit (WPU) - the processor serves all the sensor channels, and performs the servo calculations on them. The motorized mirrors are for remote beam centering. The beam shutter sends a status indication to the WPU.

4.2.3. Sensor head

The design of the wavefront sensor head and demodulation electronics is based on the prototype wavefront sensors that have been developed for the FMI (Fixed Mirror Interferometer) Alignment experiment. This hardware is described in detail in reference [8]. The rf transimpedance gain is different than for the FMI prototype, since the optical gain in LIGO is much larger. The transimpedance is chosen to match the signal levels to the mixer dynamic range - which is 1 V_{pk} at the RF input (1 dB compression point). The rf gain in the sensor head can be changed by a factor of 10;

the high gain is to be used in Detection Mode and the low gain in Acquisition Mode, when larger signals may be present and system noise is less of a concern. In Detection Mode, we are allowing a factor of 10 range between the rms rf signal level and the peak signal level (determined by input range of the mixer).

The angle sensitivity for a given sensor is defined using the root-square-sum of the angle degrees-of-freedom. From the matrix elements given in Table 3, the angle sensitivity at the mixer input in volts/radian per quad element is determined by multiplying by the following factor:

$$(0.45\ \text{A/W})\left(\frac{\text{div angle}}{10^{-5}\text{rad}}\right)(10^4\Omega)\left(\frac{1}{2}\right)\left(\sum_j M_{ij}^2\right)^{1/2} = 2.25\times10^8\left(\sum_j M_{ij}^2\right)^{1/2}\ \text{volts/rad}$$

The signal levels in the sensor heads are given in Table 4.

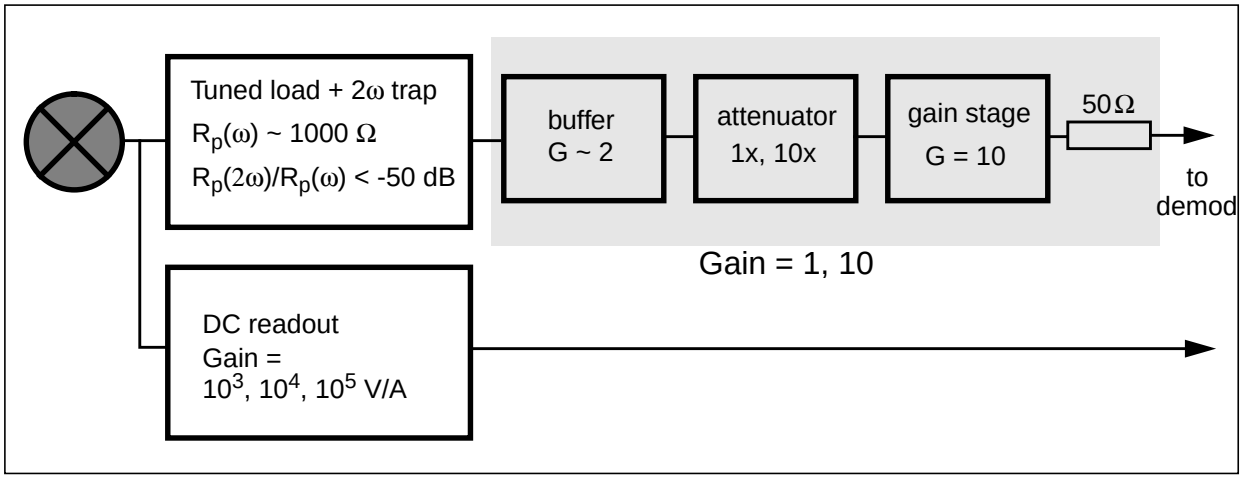

Figure 6 Electronics block diagram of a wavefront sensor head, showing the rf and dc channels for one quad-photodiode element. The blocks within the shaded box show a possible realization of the required gains based on a modification of the prototype WFS heads.

Sensor	*max rms angle, radians*	*rf-diode current, rms*	*mixer rf input, rms*	*Range = (mixer max / rms)*	*rf-diode current, 2ω, pk*	*mixer rf input, 2ω, pk*	*DC diode current*
1	10^{-8}	11 µA	0.11 V	9	55 µA	1.8 mV	64 µA
2	10^{-8}	11 µA	0.11 V	9	25 µA	0.8 mV	50 µA
3	10^{-7}	16 µA	0.16 V	6.25	0.2 mA	6.6 mV	0.4 mA
4	10^{-7}	20 µA	0.2 V	5	0.2 mA	6.6 mV	0.4 mA
5					90 µA	3.0 mV	1.9 mA

Table 4 Signal levels, *per segment of the quadrant photodiode,* for the various sensors in Detection Mode, with a transimpedance gain from photocurrent to mixer input of 10 kohm and a photodiode response of 0.45 A/W.

4.2.3.1 Photodiode

The photodiode is the EG&G model YAG-444-4A quadrant photodiode, made of near-infrared enhanced silicon. The specifications for this device are given in Table 5. The capacitance and

	Dimensions (diam./area per element/sep.) (mm/ mm^2/mm)	*Dark Current*	*Capacitance (pF)*	*Series Resistance*	*Response @ 1064 nm (A/W)*
Manufac-turer's spec.	11.4/25/0.125	75 nA max.	9	320 Ω	0.45

Table 5 Specifications for EG&G YAG-444-4A quadrant photodiode. (typical performace at 100 V bias). The specified series resistance appears to be high – our measurements show more like 80 Ω.

series resistance are compatible with the requirement of a 1 kΩ impedance of the resonant load. The diodes will be operated at a reverse bias of 100 V, at which point the capacitance is nearly independent of the bias (the plateau begins at ~90 V).

4.2.3.2 Sensor Head Test Results

The YAG-444-4A diodes were tested using an FMI WFS head, modified to accept the larger diode and for the lower RF gain as shown in Figure 6. The test setup is shown in Figure 7; the diode was illuminated with a 980 nm laser diode whose light output can be modulated up to ~100 MHz. The diode is operated at a reverse bias of –120 V. A single element was illuminated at a time with ~0.5 mW of power. A network analyzer is used to measure and tune the frequency response of each channel. The channels are tuned for 26.7 MHz by matching the phase shifts of the channels at this

frequency (resulting in the peak of the response not necessarily being at 26.7 MHz); this was done in the LO gain mode of the WFS head. Switching between elements was done by redirecting the beam with a mirror onto the chosen element, so that there was a minimum disturbance to the electronics setup.

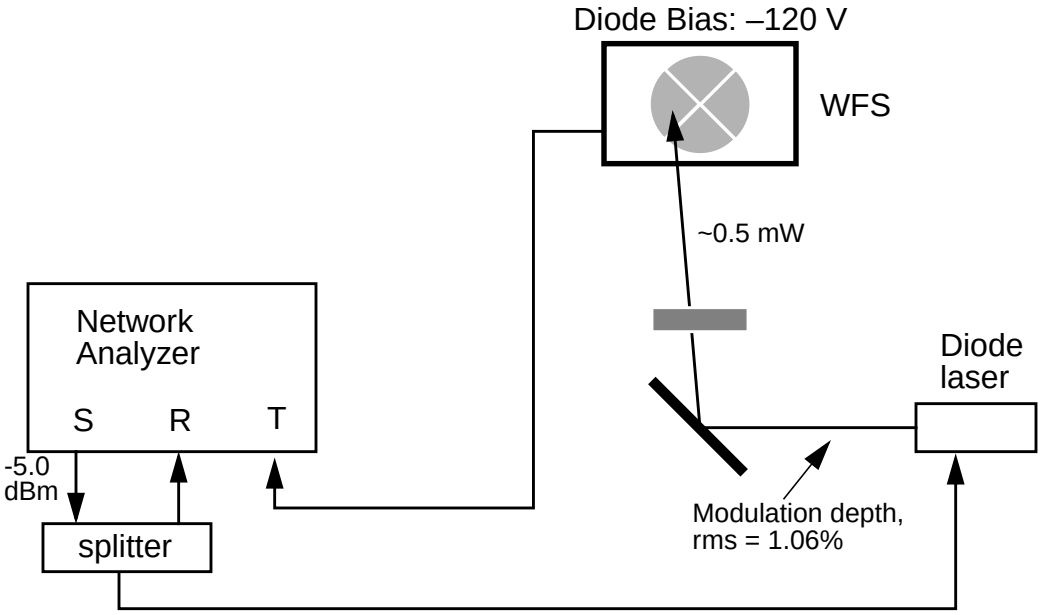

Figure 7 Test setup for RF and DC testing of a WFS head.

The RF response and the DC readout were tested; the results are given in Tables 6 & 7.

Table 6: DC and RF response for each channel as measured by the above setup.

Channel	V_{DC}	*Mag. @ 26.7 MHz*	*Phase @ 26.7 MH*	*Mag. @ 53.4 MHz*	*Peak width*
1	-276 mV	-28.5 dB	35.5°	-75 dB	3.5 MHz
2	-279 mV	-28.4 dB	35.7°	-75 dB	3.6 MHz
3	-280 mV	-28.4 dB	35.3°	-76 dB	3.5 MHz
4	-276 mV	-28.15 dB	35.5°	-77 dB	2.3 MHz

Table 7: Values of the DC readout for the channels under various conditions of illumination. The transimpedance for the DC readout is 1.0 kohm. The last two columns give the DC outputs after 10 days of operation with bias applied but no illumination (next to last column), and after 10 days of operation with 1 ma of photocurrent on element #3 (to look for increase in the dark current).

Channel	*Single Element Illuminated (mV)*				*No light (mV)*	*No light, no bias*	*Long term exposure*	
							bias only	*bias + light*
1	**-276**	4.3	4.6	3.8	-0.6	-0.6	-0.6	–
2	3.4	**-279**	2.0	4.1	-1.1	-1.0	-1.2	–
3	4.5	4.0	**-280**	4.3	-0.6	-0.6	-0.7	-0.7
4	5.7	6.0	5.9	**-276**	0.7	0.8	0.7	–

The 1.06% modulation depth and DC photocurrents in the table imply an RF photocurrent of 2.96 microamp-rms (Ch. 3). The amplitude of -28.4 dB corresponds to 3.38 mV-rms at the measurement port, giving an RF transimpedance of 1140 Ω (LO gain state), as desired.[1] The HI gain state was checked to give an additional 20 dB gain in each channel.

Cross-talk between the RF channels was also examined by illuminating one element, and measuring the signal in the channels corresponding to the adjacent and opposing elements. At this modulation frequency (26.7 MHz) the cross-coupling to the adjacent channel was -25dB, and -45 dB to the opposing channel (the cross-coupling most likely occurs in the diode). Though not very small, this level is acceptable, as the WFS scheme is relatively immune to this since the signals are formed from differences of opposing channels.

4.2.4. Noise & Error Budget

4.2.4.1 GW-band noise

In order that we do not put impractical demands on the above-band filtering, we require that the sensing noise be at least close to shot-noise limited (for post-demodulation frequencies, this applies above 40 Hz). In the case of WFS1 & WFS2, the shot noise is nearly equal to the thermal noise of the resonant tank circuit. We thus require that any electronics noise in subsequent stages does not increase the noise significantly beyond the level given by the sum of the shot noise from WFS1(2) and the tank thermal noise.

1. At this tuning frequency, a 1.5 kΩ ‘damping’ resistor is put in parallel with the load to bring the resonant impedance *down* to ~1 kΩ.

Specifically, the noise of the wavefront sensor head must be less than 7 nV/√Hz referred-to-input, or less than 70 nV/rtHz at the mixer input. The demodulator input noise must be less than 20 nV/√Hz, and the ADC input noise must be less than (G_{if} · 50 nV/√Hz), where G_{if} is the value of any post-demodulation gain (used to match the mixer output range to the ADC input range).

The equivalent angle-noise sensitivity, S_α, of a given sensor signal can be found by referring the above noise sources to the mixer input, and dividing by the angle sensitivity at the mixer input for that sensor. These numbers are given in Table 8.

WFS	*Angle Sensitivity at mixer input; per element; V/rad*	*WFS head (each channel), at the mixer input; nV/√Hz*		*Demod. input noise*	*ADC input noise*[a], *nV/√Hz*	S_α, *Equivalent angle sensitivity*[b], *rad/√Hz (f>40 Hz)*
		shot noise	*electronics noise*[c]			
1	1.1×10^7	45	70	20	50 *(f>40 Hz)*	9.0×10^{-15}
2a	1.1×10^7	40				8.8×10^{-15}
2b	1.1×10^6	40				8.8×10^{-14}
3	1.6×10^6	115				9.1×10^{-14}
4	2×10^6	115				7.3×10^{-14}
5	8.7×10^6	250				3.0×10^{-14}

Table 8 Wavefront Sensing Noise

a. Assuming +-1V ADC range, and referred to input of the pre-ADC whitening filter.
b. Since two quad elements combine to give one angle signal, the angle sensitivity given here is √2 better than for a single element.
c. Head noise RTI is thus < 7 nV/√Hz; the thermal noise of the 1kohm resonant circuit is 4.2 nV/√Hz.

4.2.4.2 Control-band Noise & Errors

Electronics Noise. In order that electronic noise in the control-band does not limit the residual angle requirement, we require that the base-band electronics noise be less than 100 μV/√Hz in the region f = 0-30 Hz, as referred to the mixer output (or mixer input, assuming a mixer gain of 0 dB). This puts the angle-equivalent integrated-rms electronics noise below 10^{-9} radian for the least sensitive sensors, and below 10^{-10} radian for the most sensitive sensors.

Offsets. A differential dc offset between two opposing channels will, if not measured and corrected for, produce an offset in the controlled angle. Referred to the mixer outputs, the differential dc offsets between opposing channels must be less than 10 mV. This ensures that the equivalent

angle offset will be below 3×10^{-9} radian for the least sensitive sensors, and below 5×10^{-10} radian for the most sensitive sensors.

The residual length deviations from resonance can also produce an alignment servo offset since the common mode rejection between opposing channels will not be infinite. However, given the fairly tight residual length requirements, this source of error was shown in the ASC Conceptual Design Document to be, *at worst*, at the 3×10^{-9} radian level (see Table 8 of the Conceptual Design).

Additional errors due to the existence of higher order optical modes (m+n >1) in the system, due to the imperfect optical surfaces, have not been analyzed fully at this time.

4.2.5. Guoy Phase Telescopes[1]

We have two constraints on the Gaussian beam at the detection plane: first, that its Guoy phase be optimized for maximum detection of the primary degree of freedom, and second, that the spot size be ‘matched’ to the size of the quadrant diode.

The spot size matching results from a trade-off between signal size and centering sensitivity; a smaller spot size implies greater sensitivity to centering errors, whereas a larger spot size is apertured by the photodiode. The dependence of the signal and errors on the spot size and photodiode shape is analyzed in reference [8]. A good solution for a photodiode without a hole is to choose the ratio of beam radius to diode diameter to be roughly 0.2. For the YAG-444-4A photodiode, this means a beam size of $\omega_{det} = 2.3$ mm at the detector.

The Gaussian beam at an output port of the interferometer is specified by a state vector

$$\begin{bmatrix} R(z_{port}) \\ w(z_{port}) \\ \eta(z_{port}) \end{bmatrix} \tag{2}$$

where $R(z_{port})$, $w(z_{port})$ and $\eta(z_{port})$ are the wavefront curvature, the spot size and the accumulated Guoy phase shift, respectively; this state vector is determined by the COS beam delivery telescopes. The state vector is then propagated through a series of lenses and propagation distances to give the desired state vector at the wavefront detector position. Operating on the state vector at the interferometer port with a cascaded series of transformations, we find the focal lengths and positions of the lenses which give the required state vector at the detector.

The Guoy phase at a given detector is chosen to maximize the signal due to misalignment of the primary degree of freedom for which it is responsible. For each detector, the magnitudes of the off-diagonal terms in the sensitivity matrix have sinusoidal dependences on the Guoy phase shift, but unlike the diagonal terms, they are usually closer to the zero of the sinusoidal variation. The

1. This section is derived in large part from reference [10].

off-diagonal terms of the alignment sensitivity matrix are thus first-order sensitive to the Guoy phase shift, while the diagonal terms are only second-order sensitive. Consequently, some care must be taken in the design and implementation of the Guoy phase telescopes.

Given the uncertainties in the focal lengths and positions of the lenses, an optimization algorithm based on a simulated annealing technique is used to minimize errors in the Guoy phase and spot size, and at the same time make the telescopes as insensitive as possible to uncertainties in their physical layout. We will attempt to use a two lens solution for the telescopes, which greatly simplifies the algorithm for optimizing the design constraints. The typical two-lens design of Guoy phase telescopes that has worked well in the Fixed Mass Interferometer (FMI) is shown in Figure 8. The first lens focuses the beam, more gently for longer focal length lenses. As the beam goes through a waist (near the focal plane), it acquires an additional 180° of Guoy phase. The second lens is placed near the waist formed by the first lens, close to the point where the beam has the desired Guoy phase. Since the spot size near the focus is very small (typically 100 μm), the second lens is usually a strong negative lens which also expands the beam; the beam thus accumulates Guoy phase relatively slowly after the second lens. This is a particularly robust scheme since the distances which are practically most difficult to control are least critical. Specifically, the design is relatively insensitive to the position of the detector, and to the position of the first lens, which is usually a few meters from the output port and can have a large uncertainty. The spacing between the two lenses is crucial, but this is typically a few centimeters and can be determined with high precision.

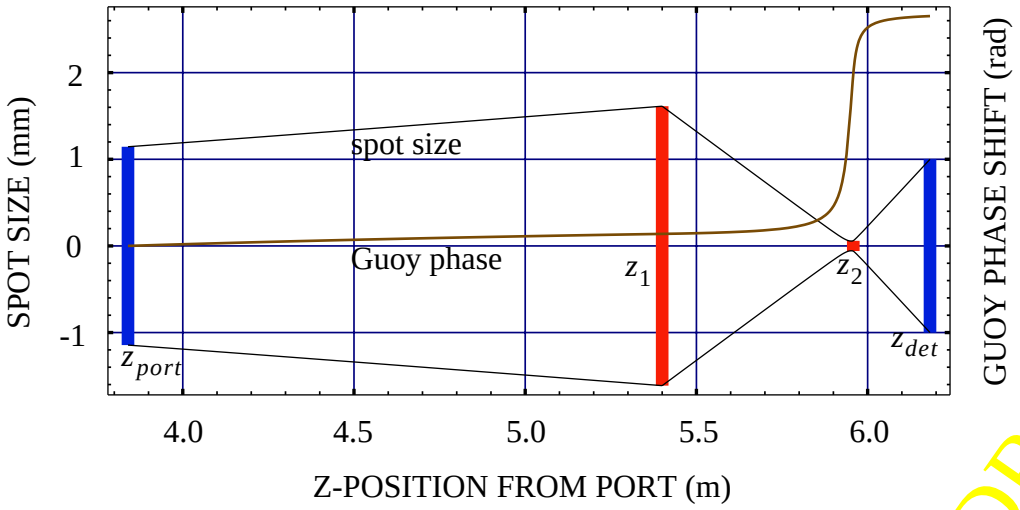

Figure 8 Beam profile and Guoy phase shift for a sample Guoy phase telescope. The spot size and guoy phase shift are plotted as a function of position from the port; z_{port} refers to the position of the port (recycling mirror in this case), z_1 and z_2 to the positions of the first (converging) and second (diverging) lenses, respectively, and z_{det} to the position of the detector.

4.3. Quadrant Position Detectors

The quadrant detectors (QPD) at the arm cavity transmission ports are designed to be useful during interferometer acquisition as well as in Detection mode. The conditions and quadrant detector requirements in each mode are given in Table 9.

The photodiodes will be the same as those currently being investigated for use in the optical levers - the CentroVision QD100-0 (responsivity: 0.13 A/W at 1064 nm) – or their 1064 nm enhanced version (-4X; responsivity: 0.45 A/W).

When the five wavefront sensor degrees-of-freedom are held to zero, the shift of the beams on the X (on-line) and Y (off-line) arms due to angular deviations of the beamsplitter (BS_α) and the input beam (IB_α) is given by (in units of fractional shift of the ETM beam per radian of optic angle):

$$\delta_X = 7.8\times10^4 \cdot IB_\alpha$$

$$\delta_Y = 7.8\times10^4 \cdot IB_\alpha - 1.6\times10^5 \cdot BS_\alpha$$

The detection sensitivity of these angles by the QPD's depends on the spot size and photocurrent at the detectors. The parameters are summarized in Table 10.

IFO State	*Power on transmission quad monitor*[a] *(photocurrent per element)*	*Quad Detector Requirements*			
		Transimpedance gain[b]	*Output noise density (f > 30Hz)*	*Output offset drift* [c]	*Bandwidth (3 dB)*
2: Recycled Michelson	3 µW (3 µA)	10 MΩ			> 100 Hz
3: Rec MI + one arm	2 µW / 90 µW (0.2 µA / 9 µA)	10 MΩ/250 kΩ			> 100 Hz
4: Detection Mode	0.1 W (max) (10 mA)	500 Ω	< 20 nV/√Hz	< 5 mV	> 1 kHz

Table 9 Quadrant Position Detector Requirements. Photocurrents assume a 1064 nm enhanced diode.

a. Assuming an ETM transmission of 10 ppm.
b. Each element; matched to ±10V output range
c. Over the temperature range and time of operation.

Parameter	*QPD-X*	*QPD-Y*
Spot size, radius	1.5 mm	
Photocurrent, per element	4 ma	
Position sensitivity at quad (left-right difference)	15 amp/meter	
Sensitivity to BS, IB angles	1.8×10^3 amp/rad	3.9×10^3 amp/rad
Shot noise	72 pA/√Hz	
Equivalent angle sensitivity	4×10^{-14} rad/√Hz	2×10^{-14} rad/√Hz

Table 10 Signal Detection parameters for the quadrant position detectors.

4.4. Servo Design

4.4.1. Detection Mode servo

The final design for the critical alignment degrees-of-freedom is essentially unchanged from the preliminary design, and is presented in the following section. We emphasis that because of the digital implementation, the servo design will be flexible. Features such as the resonant gain sections can be removed, added or changed through software.

4.4.1.1 Control loop design

A block diagram of the servo compensation (between the WFS signal and mirror torque control signal) is shown in Figure 9. The elliptic LP filter is included as part of the suspension controller;

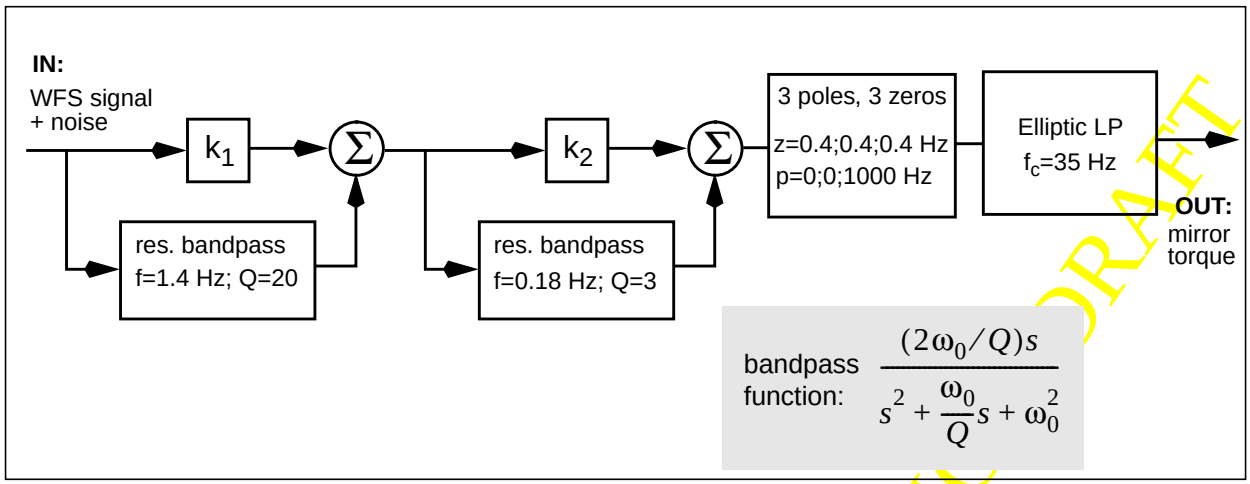

Figure 9 Block diagram of the WFS servo. The reponse of the coil driver or any signal conditioning filters are not included explicitly.

the parameters of this filter are: 4th order, 60 dB stopband, 4 dB passband ripple, 35 Hz cutoff frequency. The open loop transfer function of the complete loop is shown in Figure 10. The phase

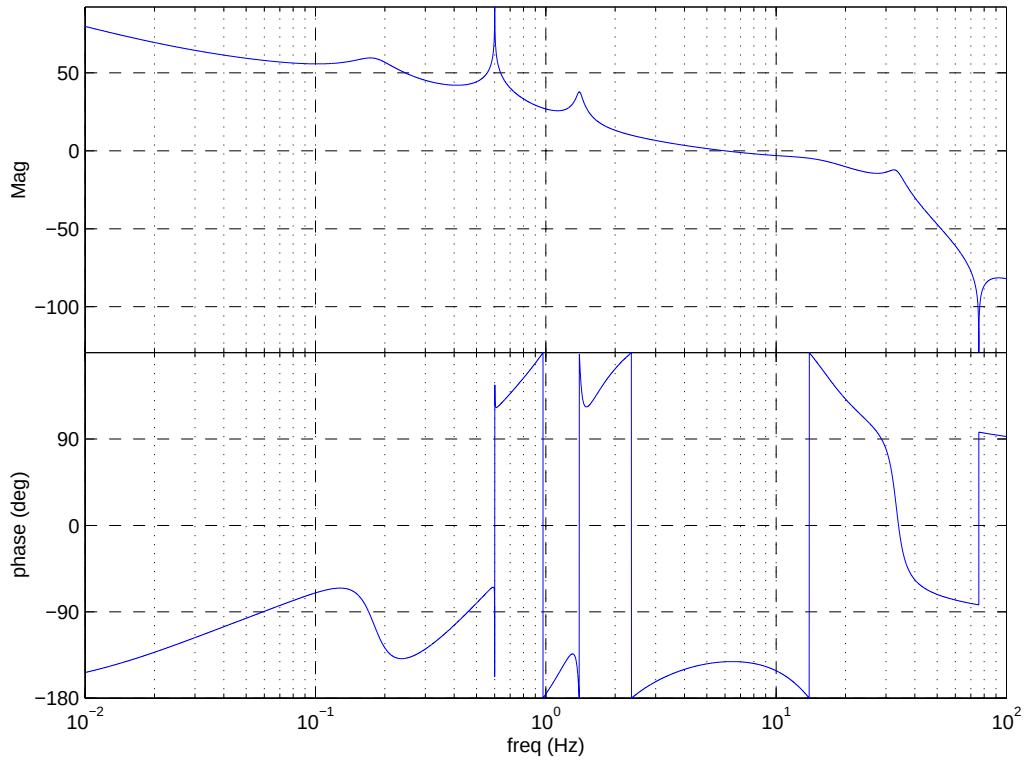

Figure 10 Open loop transfer function of a wavefront sensor control loop. Light damping of the pitch mode at 0.5 Hz is included artificially to limit the response at the resonance. Unity gain frequency is 6.0 Hz; phase margin is 38°. The 1.4 Hz resonant gain section is not required in the presence of typical WA ground motion, as shown in Figure 11.

margin is not as high as one would like, but the loop gain is a bit marginal, as shown in the next section, so any improvement in phase margin would come at the expense of increased residual deviations. The contributions to the phase lag at the unity gain frequency (on top of the 90 deg. from the 1/f response at the u.g.f.) are:

- Elliptic low-pass filter: –22.1°
- 0.18 Hz band-pass filter: –12.5°
- 1.4 Hz band-pass filter: –7.0°
- 3 zeros at 0.4 Hz (not completely compensating 2 low-frequency poles): –11.4°

4.4.1.2 Residual angle fluctuations

The residual angle fluctuations using the above servo in the presence of several ground noise inputs and leaf spring[1] stacks (Q=30; refer to reference [7] for details on the ground noise and stacks) is shown in Figure 11.

1. Model transfer functions for a stack with leaf springs were used because they were available in appropriate Matlab form; the expected stack responses for the baseline coil springs are essentially the same.

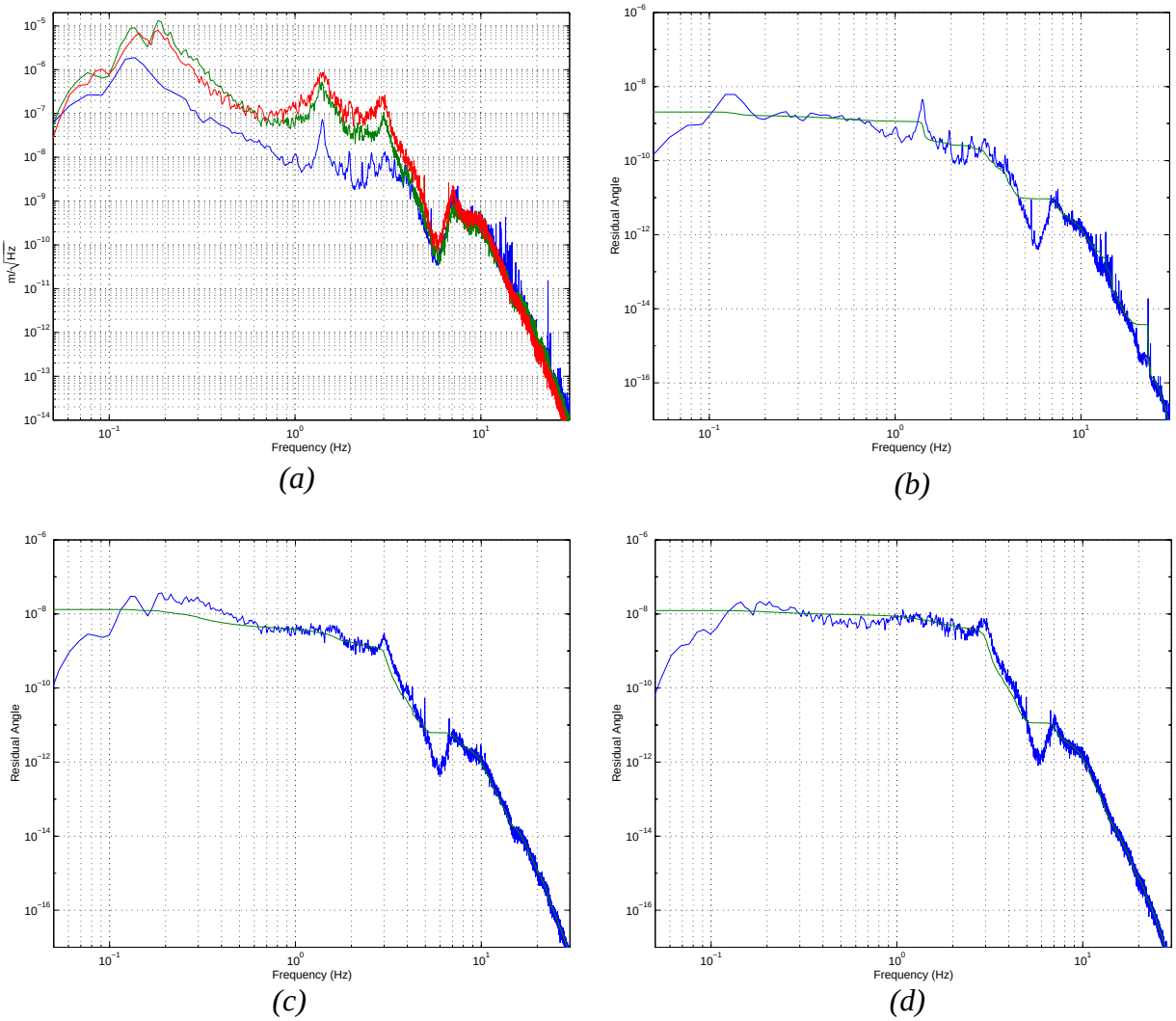

Figure 11 Residual pitch for an optic under wavefront sensor servo control. (a): Spectra of pendulum suspension point motion used to generate pitch fluctuations for LA–high microseismic peak (blue), LA–high 1-3 Hz noise (green), WA–typical (red); (b): Residual pitch using the WA input spectrum; (c) residual pitch using the LA–high microseismic peak spectrum; (d) residual pitch using the LA–high 1-3 Hz spectrum. The WA results (b) use the servo shown in Figure 10 but *without* the 1.4 Hz resonant gain stage; both LA results use the open loop gain as shown in Figure 10. The smoother line is the rms angle integrated in the band **Frequency-10 Hz** (rad_{RMS}) and the other line is the spectral density of pitch fluctuations (in rad $Hz^{-1/2}$). The integrated rms is 2.0×10^{-9} rad for (b), 1.2×10^{-8} rad for (c), and 1.3×10^{-8} rad for (d).

This model indicates that the residual angle requirement is easily met in the presence of typical WA ground motion, but is slightly exceeded in the presence of the very high ground noise that has been measured to occur in LA.

4.4.1.3 GW-band noise

In the single angular degree-of-freedom model, the mirror angle and displacement noise introduced in the GW-band by the alignment control system is:

$$\theta(f) = S_\alpha \cdot G(f)$$

$$x_m(f) = \varepsilon \cdot S_\alpha \cdot G(f)$$

where S_α is the equivalent angle sensitivity (in the GW-band) of the wavefront sensor channel (see the last column of Table 8), *G(f)* is the open loop gain, and ε is the angle → displacement cross-coupling in the suspension ($\varepsilon = \Delta x/\Delta\theta$, ratio of unintended displacement to intended angle).

Because the WFS sensitivities S_α are much worse than the GW-band angular noise requirements, high levels of GW-band (above the servo-band) filtering are needed. These filters much also be inserted in the proper places in the servos to filter out electronics noise. This filtering problem is discussed in Section 4.4.2.

Assuming we just meet the angular noise requirement, we then require that $\varepsilon \leq 3 \times 10^{-3}$ m/rad. If the cross-coupling comes only from the suspension controllers, this implies that the coil currents must be balanced to 6% or better. The SYS DRD requires the suspensions to be balanced to 1% or better; thus the requirement on the ASC contribution to the displacement noise is met.

4.4.1.4 Effect of LSC servo

The pitch angle fluctuations are dominated by displacement of the suspension point with repect to the wire take-off point (or center-of-mass, CoM) on the optic – i.e., the angle of the suspension wire, which produces a torque on the optic. The LSC servo holds the mirror's CoM fixed relative to an inertial reference frame (in our model; fixed relative to the ITM in reality); the CoM thus moves with respect to the suspension point with nearly the full microseismic peak amplitude, and the wire torque at this frequency is thus relatively large (larger than if it were just locally damped, for example).[1]

4.4.1.5 Multiple degrees-of-freedom

The modeling in the proceeding sections gives our estimate of the excitations and a servo design for a 'generic' angular pitch degree-of-freedom and wavefront sensor. This should apply well to the critical degrees-of-freedom over the 4 km baseline. Other wavefront sensor signals have less severe residual angle requirements, but poorer equivalent angle noise in the GW-band. The complete multiple-input multiple-output servo modeling has not yet been performed, but in Table 11

1. Since this coupling depends on well controlled mechanical parameters of the suspension, the effect could in principle be made less significant by imbalancing the four coil currents due to the length control signal so as to cancel the wire torque with an opposite coil-magnet torque.

we give the basic servo parameters of the various wavefront sensor signals. The approach is to

Sensor	*Sensing direction*	S_α *(rad/√Hz)*	*Filtering req.@40 Hz*	*Target servo BW, Hz*	*Target residual rms angle, rad*	*Mirrors controlled by this sensor*
WFS1	$\mathbf{u_2}$	9×10^{-15}	≥ 56 dB	6	0.8×10^{-8}	All TM's
WFS2a	$\mathbf{u_1}$	8.8×10^{-15}	≥ 56 dB	6	0.8×10^{-8}	ITM's, RM
WFS2b	$-.14\mathbf{u_1} - .4\mathbf{u_2} + .9\mathbf{u_3}$	8.8×10^{-14}	≥ 76 dB	2-3	3×10^{-8}	ITM's
WFS3	$.8\mathbf{u_1} + .13\mathbf{u_4} + .5\mathbf{u_5}$	9.1×10^{-14}	≥ 76 dB	1-2	1×10^{-7}	RM
WFS4	$.7\mathbf{u_1} - .46\mathbf{u_4} + .55\mathbf{u_5}$	7.3×10^{-14}	≥ 76 dB	1-2	1×10^{-7}	All TM's
QPD-X	**IB**	4×10^{-14}	≥ 70 dB	0.5	2×10^{-7}	IB
QPD-Y	$-.9$**BS**$+.45$**IB**	2×10^{-14}	≥ 65 dB	0.5	2×10^{-7}	BS, IB

Table 11 Sensing specifications and nominal servo parameters for each of the sensors used for alignment control. A filtering requirement of X dB means that the open loop gain must be -X dB or smaller at 40 Hz, in order to filter out the sensing noise. In this scheme, four different servo designs are used. The design used for WFS1 and WFS2a is labelled 'Servo 1', the design for WFS2b is 'Servo 2', the design for WFS3 and WFS4 is 'Servo 3', and the design for QPD-X and QPD-Y is 'Servo 4.'

keep the signals in the wavefront sensor basis for applying the servo functions and some of the low-pass filtering; then the WFS signals are combined to give torque control signals which are

sent to the PITCH and YAW inputs on the suspension controllers. A block diagram of this scheme is shown in Figure 12.

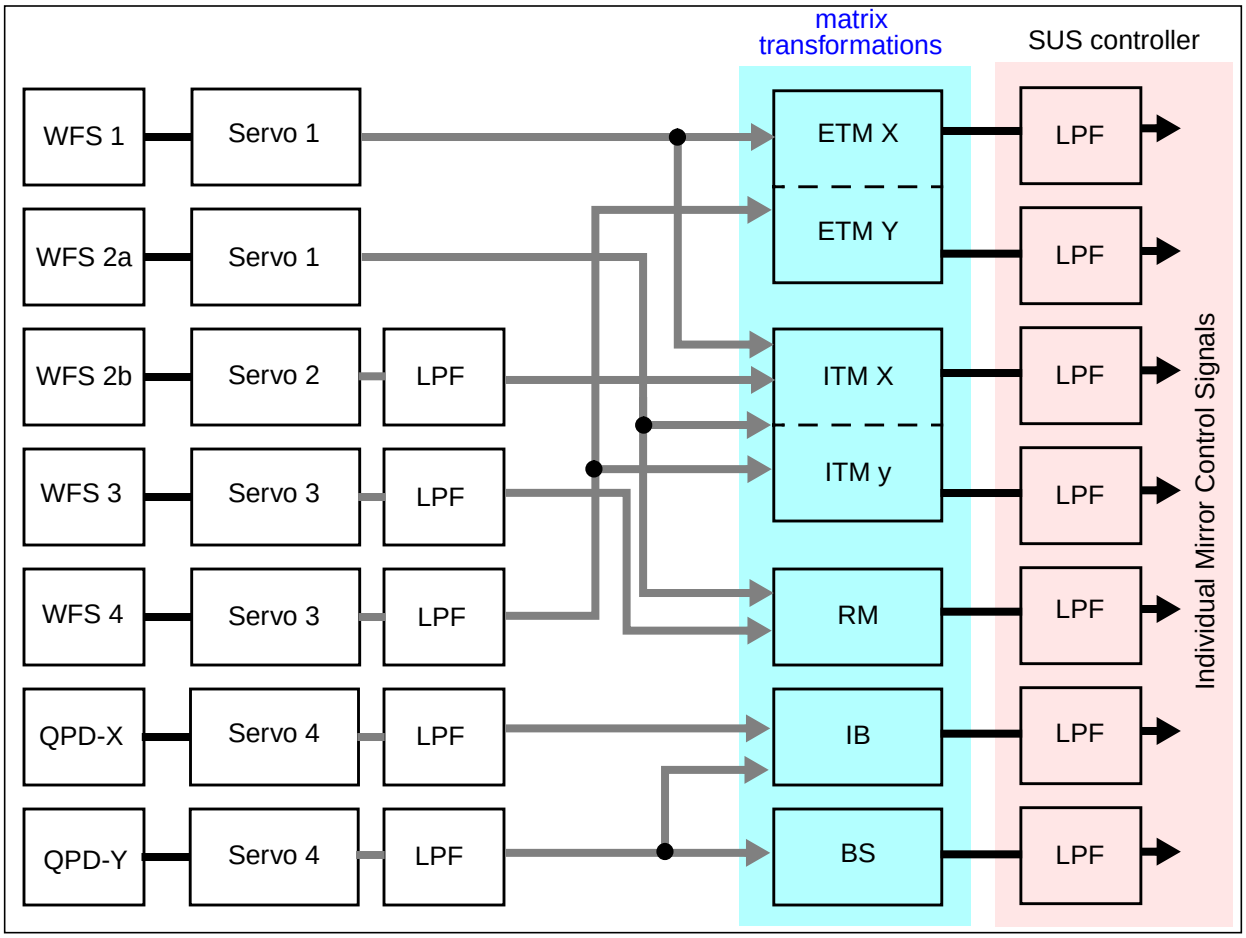

Figure 12 Block diagram of nominal multiple degree-of-freedom servo, where the servo functions are applied in the basis in which the alignment signals are sensed. The final low-pass filter (LPF) is the suspension controller elliptic filter. The bottom four channels have additional low-pass filtering (implemented in software) in order to meet the filter requirements given in Table 11. The servo definitions are given in Table 11.

A trial design for ‘Servo 2’ is shown in block form in Figure 13. This servo uses a bandstop filter to achieve more filtering in the 40-70 Hz band. ‘Servo 3’ and ‘Servo 4’ are either similar or simpler, so we do not present designs of these.

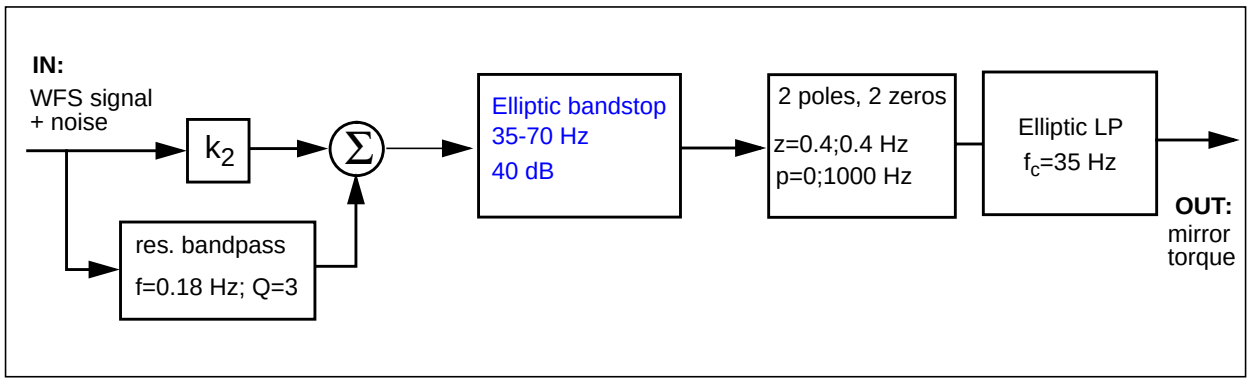

Figure 13 Block diagram of a 'Servo 2' design. With a unity gain frequency of 3 Hz (phase margin of 35 deg) the residual angle predicted using the LA–high microseismic peak input is 6×10^{-8} rad-rms, and 1×10^{-8} rad-rms using the WA-typical input. The 6th order elliptic bandstop filter would be implemented with a digital filter.

4.4.1.6 Actuation Range

The servo modeling shows that the angular correction in the single degree-of-freedom model is about $\pm 10^{-5}$ rad, dominated by corrections at the microseismic peak (see reference [11]). It is so large due to the length-angle cross-coupling effect described in section 4.4.1.4 above. For frequencies $f < 10$ mHz, the worst case stack drift in yaw of 8×10^{-10}rad/sec ([12]) determines the range requirement: in order that we have sufficient angular control to maintain alignment over ~10 days, the full suspension angular actuation range of ~1 mrad p-p is required.

4.4.1.7 Comparison with requirements

The requirements for residual angle deviations are given in Table 12 in the *u* basis. Given the

Direction	*Residual Angle, radians rms*	*Shot noise sensitivity degradation (%)*
u_1	0.8×10^{-8}	0.21
u_2	0.8×10^{-8}	0.25
u_3	3×10^{-8}	0.015
u_4	1×10^{-7}	0.02
u_5	1×10^{-7}	0.003
	SUM	0.5

Table 12 Residual angles requirements.

modeling results presented above, we estimate the residual angle requirements will be met with some margin in the presence of typical WA ground motion. In the presence of 'high Louisiana ground noise,' however, these levels will be slightly exceeded (worst case of 1% shot noise degradation is estimated).

4.4.2. Signal Conditioning

Table 8 calls for an ADC range/(noise) ratio of 1V-pk/(50 nV/√Hz), referred to the input of the whitening filter. The actual range/noise of the Pentek 6102 ADC module that will be used is 10V-pk/(30 μV/√Hz). Thus a whitening factor of > 60 is required (whitening factor refers to the ratio of the gain at f >40 Hz to the gain at DC in the whitening filter), in addition to an overall gain of 10. Some dewhitening at the output of the DAC (in addition to the low-pass filtering in the suspension controller) will also be required to suppress DAC noise.

The complete signal conditioning design for all WFS channels will be performed as part of the ASC CDS final design, with the aid of a complete closed loop model of all channels. In lieu of this, we present here a single channel, open-loop model to indicate the kind of design that will be needed to meet the requirements. This model is given in Figure 14, which shows the signal chain between angle input at the WFS to angle output at the optic. The sensing & control noise requirement is met at 60 Hz, as indicated in the figure. Applying the same model at 40 Hz, however, indicates that the noise is about a factor of 10 above the requirement; the problem is that the suspension controller elliptic filter only gives -16 dB of attenuation at 40 Hz. Since the measured DAC noise (as shown in Figure 14) is relatively small, we could add a stopband filter, with attenuation of 20-25 dB, in the

digital domain and come very close to the requirement; such a filter will have some effect on the phase margin though.

4.4.3. Acquisition servo

A servo mode will be provided for each WFS control channel where the loop response is an unconditionally stable 1/*f* response from DC (or very low frequency), up until the suspension controller elliptic LPF becomes effective.

4.5. Mode Cleaner Alignment Design

4.5.1. Initial Alignment

Initial alignment of the mode cleaner is covered under the Input Optics Final Design.

4.5.2. Alignment Acquisition

The input beam to the mode cleaner must first be aligned well enough so that the MC can be locked on the TEM_{00} mode (input beam angle and position should be within ~1/3 of the MC divergence angle and beam waist, respectively). This will be done by the monitoring spot patterns on the MC mirrors and of the transmitted beam, and manually controlling the input beam direction until the patterns collapse to something close to a TEM_{00} mode. We expect this procedure will need to be done only once at the outset (or if there is a major perturbation to the input beam direction).

The results of modal modeling and prototype experience have both shown that once length control (cavity resonance) is achieved, proper wavefront sensor signals exist for bringing the cavity into optimal alignment. Thus once the MC is resonant, the wavefront sensor loops will be closed.

4.5.3. Detection Mode Alignment

The absolute alignment requirement for the MC is much more tolerant than for the interferometer. The MC beam divergence angle is 200 μrad, and controlling each degree-of-freedom to within 5 μrad of optimal will ensure that the TEM_{00} mode coupling is > 99%.

Wavefront sensors will be used to detect the misalignments of the mode cleaner [T960118-00-D]. The preliminary design proposal to use the non-resonant sidebands, de-tuned somewhat from the mode cleaner free-spectral-range, has been changed in favor of generating a separate RF phase modulation used only for length and alignment control of the mode cleaner.

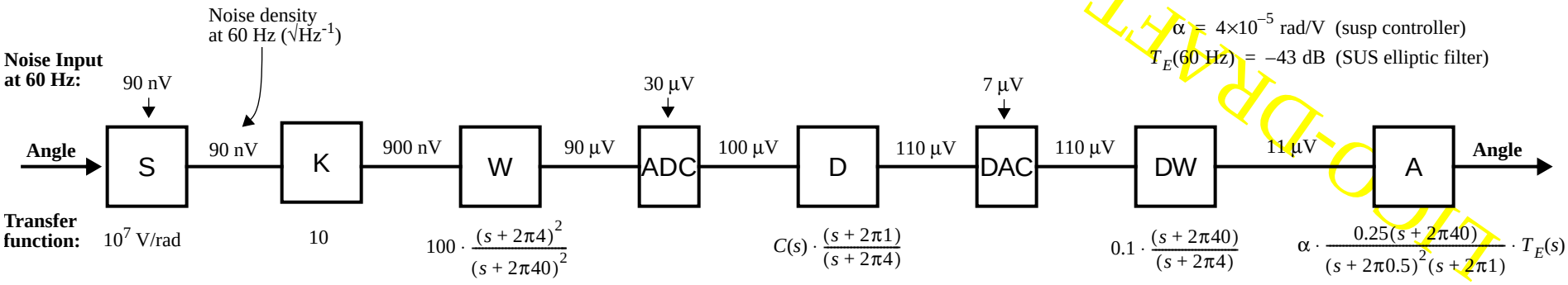

Gain at 60 Hz: $10^7 \times 10 \times 100 \times 4 \cdot C(60\text{Hz}) \times 0.1 \times \alpha \cdot \left(\frac{0.5}{60}\right)^2 \cdot \frac{1}{40} \cdot T_E(60\text{Hz})$

$= 0.28 \cdot C(60\text{Hz}) \cdot T_E(60\text{Hz})$,

which should equal: $0.08 \cdot T_E(60\text{Hz})$, for a unity gain frequency of 5 Hz $\Rightarrow C(60\text{Hz}) = 0.29$

Angular noise at 60 Hz:

$$11 \frac{\mu\text{V}}{\sqrt{\text{Hz}}} \cdot \alpha \cdot \left(\frac{0.5}{60}\right)^2 \cdot \frac{1}{40} \cdot T_E(60\text{Hz}) = 5.4\times10^{-18} \text{ rad}/\sqrt{\text{Hz}}$$

Requirement at 60 Hz: $\leq 7\times10^{-18}$ rad/$\sqrt{\text{Hz}}$

Figure 14 Signal chain for single degree-of-freedom model of a WFS channel. S = sensor gain; K = gain factor; W = whitening filter; ADC = analog-digital converter; D = digital processor; DAC = digital-analog converter; DW = dewhitening filter; A = actuator (includes pendulum dynamics & coil driver response, including elliptic low-pass filter). This open loop model is a valid approximation in the GW band, since the total open loop gain is less than unity. The numbers above a block indicate the voltage noise added at that point; the numbers above the connecting lines indicate the noise in the chain at that point. The transfer function $C(s)$, in the 'D' block, corresponds to the WFS controller response, as given for example in Figure 9, not including the elliptic LPF function. The calculation here shows that the sensing & control noise requirement is met at 60 and above (the sensing & control noise rolls off faster than the requirement above 60 Hz).

The servo system serves to find the optimal alignment and control against drifts; the loop design will have a simple one-pole response, and a maximum bandwidth of 1 Hz. Control will be applied to the input beam direction, via steerable mirrors in the IOO (outside the vacuum); see Figure 15.

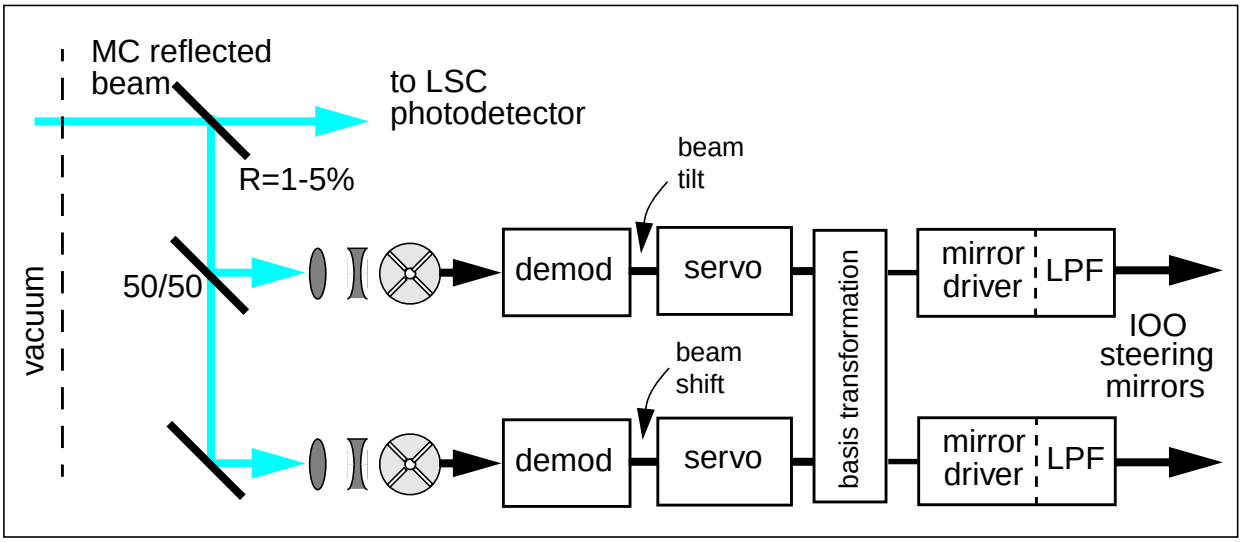

Figure 15 Alignment Control system for the mode cleaner. One WFS detects shifts of the input beam and one detects tilts, with respect to the waist position. The low pass filters (LPF) after the mirror drivers serve to filter electronic noise in the GW-band.

4.6. 2 km Interferometer

The design of the ASC system for the 2 km interferometer is nominally the same as for the 4 km interferometer. The two additional optics (the folding mirrors) will need to be included in the initial alignment procedure. In Detection mode, the folding mirrors will be locally damped (in angle).

The GW-sensitivity to misalignment, and the wavefront sensor signals for the 2 km interferometer have been calculated and are found in references [4] and [9], respectively. The differences between the 2 km and 4 km systems are small (except for the modulation frequencies); no separate design is needed for the alignment control system of the 2 km interferometer.

5. DIAGNOSTICS

For the diagnostics design of the ASC, please refer to the following documents: *Global Diagnostics Preliminary Design*, T970172-A-D, which describes the diagnostic tools and testing utilities that will be available, as well as some specific ASC tests (especially section C..2.11 of that document); and *GDS Reflective Memory Organization*, T980020-00-D, which describes the system of digital test points in the ASC.

Diagnostic tests on or involving the ASC are outlined in Table 13.

APPENDIX 1 DEFINITIONS AND PARAMETERS

The interferometer parameters used for the calculations in this document are listed in Table 14, and the properties of the interferometer sensitivity covariance matrix are listed in.

Parameter	Unit	arm (ITM)	arm (ETM)	recycl. (RM)
length (common / differential)	m		3999.01	9.38/0.21
power transmission	%	3	0.0015	2.44
losses	ppm			
radius of curvature	m	-14,571	7400	-9998.65
modulation frequencies	MHz		23.97	35.96 (NR)
modulation depths	Γ		0.45	0.045
wavelength	μm	1.064		

Table 14 Interferometer parameters used in the modeling.

Name	*eigenvector (ellipsoid axis)*					*eigenvalue* σ_i^2
	ΔETM	ΔITM	$\overline{ETM}$	$\overline{ITM}$	RM	
u_1	0	0	0	**-0.58**	**0.81**	-0.00061
u_2	**0.91**	**0.42**	0	0	0	-0.0005
u_3	**-0.42**	**0.91**	0	0	0	-0.116
u_4	0	0	**0.92**	**0.32**	**0.23**	-0.834
u_5	0	0	**0.39**	**-0.75**	**-0.54**	-6.39

Table 15 Covariance Matrix. Eigenvalues (variances) and eigenvectors (axes of direction of variance ellipsoid) of the signal-to-noise matrix.

APPENDIX 2 ASC CHANNEL COUNT

A list of the ASC channels being sampled by DAQS may be found in *LIGO Channel Count*, LIGO-T980004.

APPENDIX 3 REFERENCES

[1] LIGO-T960112-05-D, *Detector Subsystems Requirements.*

[2] LIGO-T950072-00-R, *Evaluation of proposed changes to the suspension sensor electronics.*

[3] LIGO-T960005-00-R, *Principles of Calculating Alignment Signals in Complex Resonant Optical Interferometers.*

[4] LIGO-T960114-B-D, *Modal Model Update 2, GW Sensitivity to Angular Misalignments.*

[5] LIGO-T960085-00-D, *LSC Configuration Issues*

[6] LIGO-T960065, *Seismic Isolation Design Requirements Document*, section 2.5.5.

[7] LIGO-T960103-00-D, *ASC: Environmental Input to Alignment Noise.*

[8] LIGO-T960111-A-D, *Wavefront Sensor.*

[9] LIGO-T960115-A-D, *Modal Model Update 3, Small Angle Regime.*

[10] *Alignment Issues in Laser Interferometric Gravitational-Wave Detectors*, Nergis Mavalvala, Ph.D. Thesis, M.I.T., January 1997.

[11] LIGO-T97xxxxx, *Comparison of forces and torques from feedback servos for the LSC and ASC.*

[12] LIGO-T960065-02-D, *Seismic Isolation Design Requirements Document.*

[13] LIGO-T960728-00-D, *Requirements of the LOS suspension Driver.*

[14] LIGO-T970058-00-D, *Modal Model Update 7, Angular Transfer Functions.*

	Diagnostics	*Type*	*Condition*	*Drive*	*Measurement*	*Monitor*	*Analysis*	*Action*
1	Sensitivity Matrix	external	detection mode	ifo mirror angles sine: 50–200 Hz 10^{-13} to 10^{-12} rad	WFS	SUS sensors opt. lev.	Fourier	update ASC servo matrix & rf phases
2	Centering	external	detection mode	bs & ib direction sine: <1 Hz 10^{-7} to 10^{-6} rad	QMPU bs & ib control	WFS SUS sensors opt. lev.	Fourier	update ASC servo matrix
3	Angle-length coupling	external	detection mode	ifo mirror angles sine: 50–200 Hz 10^{-13} to 10^{-12} rad	LSC signals	WFS SUS sensors opt. lev.	Fourier	adjust transverse mirror positions
4	Input beam jitter coupling	external	detection mode	ib direction sine: 50–200 Hz 10^{-13} to 10^{-12} rad ifo mirror angles static: ~10^{-7} rad	LSC signals (dark port)	WFS SUS sensors opt. lev.	Fourier	update ASC servo offsets
5	Maximum GW sensitivity	external	detection mode	ifo mirror angles static: grid diff. length, e.g. 150 Hz, 10^{-17} m	power LSC signals	WFS SUS sensors opt. lev.	Average Fourier	update ASC servo offsets
6	Mode matching	external	detection mode	mode matching telescope	power	cameras	Average	adjust telescope
7	Frequency response	external	detection mode	ifo mirror angles ib direction step: 1–10 s	WFS angle controls	WFS SUS sensors opt. lev.	Average	update ASC servo bandwidth
8	Transient	external	acquisition mode	seismic	WFS, power LSC signals	SUS sensors opt. lev.	Time series	get smart
9	Photodiode calibration	internal	setup mode	light bulb	WFS (dc & rf)		Fourier	adjust ASC calibration corrections

Table 13 ASC Diagnostic Tests